Research Article

J. Electrochem. Sci. Technol., **2024**, *15(4), 541-550*

Morphological Modulation of TiO_2 Nanotube via Optimal Anodization Condition for Solar Water Oxidation

Jiwon Heo[1], Kai Zhu[2], Jun-Seok Ha[1,3]*, and Soon-Hyung Kang[3,4]*

[1]*School of Chemical Engineering, Chonnam National University, Buk-gu, Gwangju 61186, Republic of Korea*
[2]*Chemistry and Nanoscience Center, National Renewable Energy Laboratory, Golden, CO 80401, USA*
[3]*Optoelectronics Convergence Research Center, Chonnam National University, Gwangju 61186, Republic of Korea*
[4]*Department of Chemistry Education, Chonnam National University, Gwangju 61186, Republic of Korea*

ABSTRACT

With the depletion of fossil fuels and the rising global demand for energy, photoelectrochemical (PEC) water splitting presents a promising solution to avert an energy crisis. Titanium dioxide (TiO_2), an *n*-type semiconductor, has gained popularity as a photoanode due to its remarkable PEC properties. Nevertheless, inherent challenges such as a wide band gap (~3.2 eV), charge recombination, and slow oxygen evolution reaction (OER) rates at the surface limit its practical application by constraining light absorption. To overcome these limitations, we have developed TiO_2 nanotubes (NTs) using a facile anodization method. This study examines the impact of anodization growth parameters on solar water oxidation performance. Specifically, TiO_2 NTs with modified anodization time (referred to as TiO_2-6) showed a 3.5-fold increase in photocurrent density compared to the as-grown TiO_2 NTs. Furthermore, electrochemical analyses, such as electrochemical impedance spectroscopy (EIS), indicated a significant decrease in charge transfer resistance following the adjustment of on-off anodization time. Additionally, the TiO_2-6 photoanode demonstrated a higher electrochemically active surface area (ECSA) than other samples. Therefore, optimal nanostructuring parameters are crucial for enhancing the PEC properties of TiO_2 NTs. Overall, our findings offer valuable insights for fabricating high-quality TiO_2 NTs photoanodes, contributing to developing efficient PEC systems for sustainable energy production.

Keywords : PEC water splitting, Titanium Dioxide, Nanotubes, Photoanode, Oxygen evolution reaction

Received : 14 June 2024, Accepted : 23 July 2024

1. Introduction

As global energy demand rises, transitioning from fossil fuel-based energy sources to sustainable alternatives is crucial. In this context, photoelectrochemical (PEC) water splitting has emerged as a promising technology for producing hydrogen (H_2) that can reduce the reliance on existing energy sources. However, the current H_2 production mainly depends on gas reforming methods, contributing to CO_2 emissions and global warming [1–3]. On the other hand, H_2 production through solar water splitting is environmentally friendly, producing no harmful byproducts and causing minimal resource depletion. However, the process of solar-based water splitting into H_2 and O_2 requires substantial energy due to the need for redox reactions at each electrode, which are hampered by charge transfer overpotential as well as the fast recombination at each interface [4–6]. To address these challenges, developing efficient photoelectrodes to match the solar spectrum and finding suitable material combinations to suppress charge recombination is paramount.

Titanium dioxide (TiO_2) has long been recognized as a promising candidate for photocatalysis and PEC applications, including solar water splitting, due to its excellent stability and environmental benignity [7–11]. Despite these advantages, TiO_2's application in PEC water splitting is limited by a large band gap, restricting light absorption to the ultraviolet (UV) range, representing only a small portion of the solar

*E-mail address: jsha@jnu.ac.kr (J.-S. Ha),
skang@jnu.ac.kr (S.-H. Kang)

DOI: https://doi.org/10.33961/jecst.2024.00626

spectrum. In addition, the rapid recombination of photo-generated electron-hole pairs greatly reduces the quantum efficiency of the PEC process [12,13]. Accordingly, various material combinations and engineering approaches have been proposed to enhance TiO_2-based PEC performance.

Anodization has been identified as an effective method to improve the PEC performance of TiO_2 photoanodes, creating self-ordered TiO_2 nanotubes with one-dimensional (1D) nanostructures. This technique enhances charge separation and transfer efficiency at the electrode/electrolyte interface [14–16], significantly increasing the surface area and modifying the electronic properties of TiO_2, which are crucial for optimizing its functionality in PEC applications. For instance, research by Lin et al. highlights the fabrication of high specific surface area TiO_2 nanopowders through the anodization of porous titanium, leveraging TiO_2's unique electronic and optoelectronic properties and catalytic capabilities essential for efficient water splitting [17]. Similarly, Q. Qian and colleagues demonstrated the potential of using internally anodized porous titanium to create immobilized TiO_2 nanotubes [18], which, with their high specific surface area, enhance electrochemical interactions within the PEC system, boosting overall photoelectrochemical activity. Sun and Yan's study reveals how varying anodization voltage can alter the length and density of TiO_2 nanotubes, directly impacting hydrogen production efficiency in a two-compartment photoelectrochemical cell [19]. Another study by Zhong et al. shows that larger nanotube diameters, achieved through specific anodization conditions, can significantly enhance the surface area and, consequently, the photocatalytic activity of TiO_2 structures [20].

In this study, we explored the optimal anodization conditions for TiO_2 nanotube (NT) photoanodes to enhance their performance in PEC water splitting, making hydrogen production more efficient and effective. By thoroughly examining photocurrent density, electrochemical impedance spectroscopy (EIS), and Mott-Schottky analysis, we investigated the synergistic effects between anodization parameters and the PEC properties of TiO_2 photoanodes. Particular attention was given to the roles of electrochemically active surface area (ECSA), charge transfer resistance, and onset potential in determining the efficiency of the PEC water-splitting process. This comprehensive analysis provides insights into designing high-efficiency photochemical systems for hydrogen production and elucidates the underlying mechanisms contributing to the enhanced PEC activity of TiO_2 photoanodes, aiming to advance the field of sustainable energy research. This also supports the broader goal of reducing reliance on fossil fuels and mitigating the effects of climate change by transitioning to sustainable energy sources. The enhanced PEC activity of TiO_2 photocathodes developed in this study represents an important step forward in the field of solar-based hydrogen production and provides a promising pathway toward clean and sustainable energy solutions.

2. Experimental

2.1 Growth of TiO_2 nanotubes (NTs)

Initially, Ti plates were cleaned with acetone and washed with ethanol and deionized (DI) water to remove surface impurities. The plates were then dried using a nitrogen gas flow. The anodization process was conducted under various voltage conditions in an electrolytic solution comprising 97 wt% ethylene glycol, 3 wt% DI water, and 0.3 wt% ammonium fluoride. For the reference sample, a constant voltage of 60 V was applied for 20 min. For the TiO_2-6 sample, an on-off anodization procedure was employed: 60 V for 3 min (on), followed by 20 V for

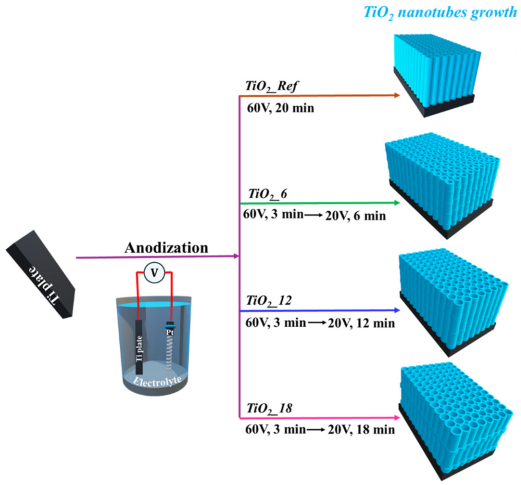

Scheme 1. Schematic diagram to describe how to modulate the applied voltage to develop (a) TiO_2-ref, (b) TiO_2-6, (c) TiO_2-12, (d) TiO_2-18 film.

6 min (off), repeated in 10 cycles. Similarly, TiO_2-12 samples were subjected to 60 V for 3 min (on), then 20 V for 12 min (off), repeated in the same cycles. Finally, the TiO_2-18 sample underwent 60 V for 3 min (on), followed by 20 V for 18 min (off), under identical cycles. After anodization, the samples were rinsed with DI water and air-dried. The voltage profiles for each anodization process correspond to TiO_2-ref, TiO_2-6, TiO_2-12, and TiO_2-18 samples, as briefly depicted in Scheme 1, with specific voltage patterns applied over time detailed in Fig. S1 (in supporting information).

2.2 Materials characterizations

The surface and cross-sectional morphology of the synthesized TiO_2 photoanodes were examined using field emission scanning electron microscopy (FE-SEM) (Hitachi, SU5000) at Energy Convergence Core Facility in Chonnam National University. The optical properties were assessed through UV-visible spectroscopy (PerkinElmer, Lambda 365), while the crystalline characteristics were determined using X-ray diffraction (XRD) (EMPYREAN/Malvern Panalytical) at Energy Convergence Core Facility in Chonnam National University.

2.3 PEC experiments

PEC water-splitting experiments were conducted in a three-electrode cell configuration. The fabricated photoanode served as the working electrode (WE), a Pt wire acted as the counter electrode (CE), and a saturated Ag/AgCl reference electrode (RE) with 3 M KCl was used. The electrodes were immersed in a 0.1 M sodium hydroxide (NaOH) solution as the electrolyte. Illumination was provided by a 300 W Xenon (Xe) arc lamp (Newport), delivering a light intensity of 100 mW cm^{-2}. Linear sweep voltammetry (LSV) measurements were performed at a scan rate of 50 mV s^{-1}. The measured potential ($E_{Ag/AgCl}$) was converted to the reversible hydrogen electrode (RHE, E_{RHE}) scale using the following equation [16,21]:

$$E_{RHE} = E_{Ag/AgCl} + 0.059 \times pH + 0.1976 \quad (1)$$

To further investigate the charge transfer properties of the photoanodes, EIS was carried out within the frequency range of 1 Hz to 10 kHz under open-circuit conditions and both illuminated and dark conditions. Additionally, cyclic voltammetry (CV) was conducted to evaluate the ECSA, which compares the active surface area available for solar water splitting reactions.

3. Results and Discussion

The surface and cross-sectional morphological properties of TiO_2 nanotube arrays were compared using FE-SEM images summarized in Fig. 1. All samples displayed a one-dimensional nanotubular structure. The control sample, TiO_2-ref, exhibited a pore diameter of approximately 53 nm and a length of about 8.5 m, with uniform nanopores through the surface area and no observed inter-spacing between the nanopores, indicating a strong interaction. Conversely, TiO_2-6, TiO_2-12, and TiO_2-18 nanotube arrays, fabricated by pulsed anodization through a repeated on (60 V)–off (20 V) cycle, showed segmented bamboo-like structures. Herein, the several key parameters to characterize the TiO_2 nanotubes can be defined. Thickness means the wall thickness of the nanotubes. Spacing indicates the distance between adjacent nanotubes. Pore size denotes the diameter of the openings at the top of the nanotubes. Segment length (node) is the length of each segment within the nanotube structure. To elucidate the differences in nanostructures induced by pulse duration, the pore size, segment length (node), and nanotube wall thickness were measured at 50 different points for each sample, and the average values were summarized in Table 1. Longer off-time anodization resulted in longer TiO_2 nanotubes, extended node lengths, and larger pore sizes. This bamboo-like TiO_2 nanotube structure enhances the active surface area compared to planar TiO_2 nanotubes, facilitating easier electrolyte insertion and improving charge carrier diffusion during the solar water splitting process. This quantitative analysis provides clear insight into the impact of pulse duration on the structural properties of TiO_2 nanotubes, confirming that anodization parameters significantly affect morphology and potentially the PEC performance of TiO_2 nanotube-based systems.

The crystal structure of TiO_2 photoanodes fabricated using various anodization methods was characterized through XRD analysis. The resulting XRD patterns, displayed in Fig. 2, confirm that all four samples comprise the ana tase TiO_2 phase [22,23].

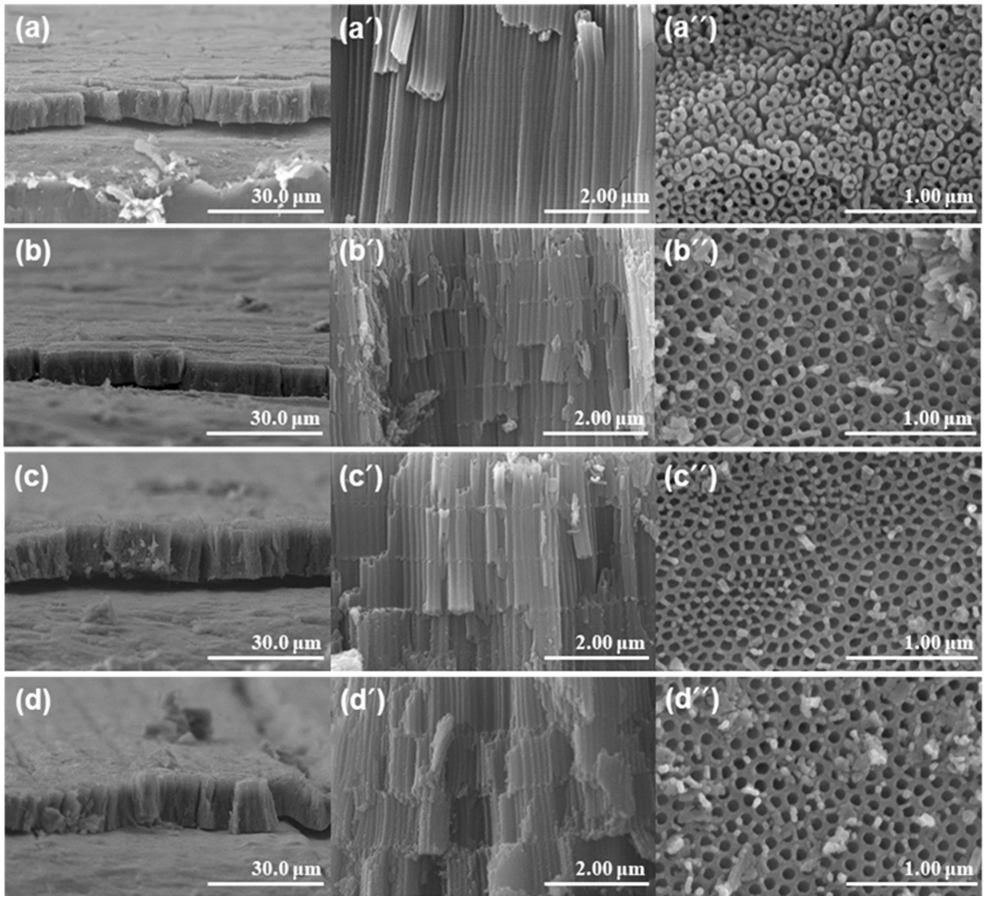

Fig. 1. FE-SEM images showing the cross-section and surface morphology of TiO_2 NTs, with (a, a') cross-sectional views of TiO_2-ref, (a") surface view of TiO_2-ref, (b, b') side views of TiO_2-6, (b") surface view of TiO_2-6, (c, c') cross-sectional views of TiO_2-12, (c") surface view of TiO_2-12, and (d, d') cross-sectional views of TiO_2-18, (d") surface view of TiO_2-18.

Table 1. Summary of the geometric parameters of TiO_2 NTs shown in Fig. 1

Photoanode	Thickness (m)	Spacing (nm)	Pore size (nm)	Wall thickness (nm)
TiO_2-ref	8.5	0	52.7	49.6
TiO_2-6	8.7	832	89.7	22.3
TiO_2-12	9.9	1132	91.3	27.6
TiO_2-18	12.7	1240	105.3	38.9

Notably, prominent peaks were observed at 25.3° and 48.1°, corresponding to the major (101) and (200) planes of anatase TiO_2, respectively [24]. As the off-time during electrochemical anodization increased, the peak intensity of the (101) plane slightly increased, indirectly indicating a longer growth of the TiO_2 nanotube arrays. This result demonstrates that all samples possess the anatase TiO_2 crystal structure, confirming the successful synthesis of anatase phase TiO_2 photoanodes through anodization.

The optical properties of the TiO_2 nanotube arrays were analyzed using UV-visible (UV-Vis) spectroscopy (Fig. 3), revealing that the strongest absorption occurred predominantly in the UV region. Specifically, light absorption began at 400 nm, with intensity steadily rising with longer off-time anodization. For

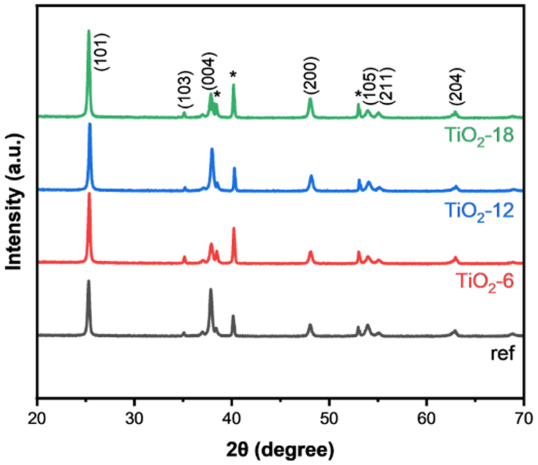

Fig. 2. XRD patterns of TiO_2 NTs, including * peaks from the Ti substrate.

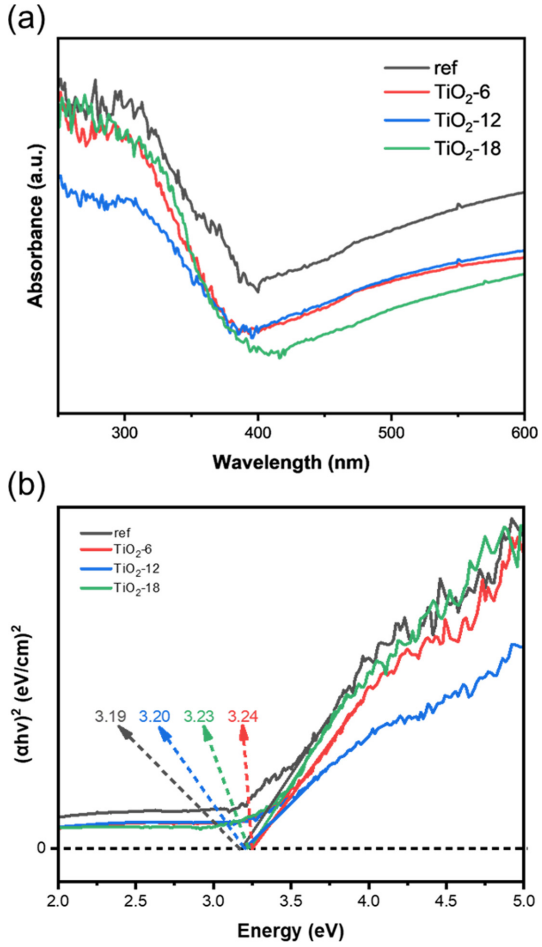

Fig. 3. Optical characterization of TiO_2 NTs: (a) absorbance spectra and (b) Tauc plots.

the sample with an 18-min off-time anodization, a slight visible absorption around 420 nm was observed, potentially resulting from the formation of defect or trap-based sub-bands [25,26].

To compare the optical bandgap of each sample, Tauc plots were derived using the following equation (2) [27–29]. The TiO_2 bandgap was calculated to be approximately 3.2 eV. Compared to the control TiO_2 sample, the TiO_2 nanotube arrays produced through pulse anodization exhibited a slightly increased bandgap, likely due to the removal or passivation of defect or trap sites [30–32].

$$(\alpha h\nu)^2 = 2.303 \times absorbance \times E \quad (2)$$

In conclusion, all samples demonstrated optical properties consistent with TiO_2 [29,33,34].

To calculate the Electrochemically Active Surface Area (ECSA), Cyclic Voltammetry (CV) measurements were conducted at scan rates ranging from 25 mV s^{-1} to 150 mV s^{-1}, increasing in increments of 25 mV s^{-1}. The measurements were performed within a voltage range of –0.3V to 0.5V versus Ag/AgCl, being in the non-faradaic region and ensuring that the measured currents are primarily due to double-layer charging rather than faradaic processes [26,35,36]. These values were then converted to V versus RHE using the Nernst Equation (Eq. 1). Two key parameters, C_s and C_{dl}, are used to determine the ECSA. C_s represents the specific capacitance of an ideal flat surface of the electrocatalyst, with a commonly used mean value of 0.04 mF cm^{-2} in calculations [37,38]. C_{dl}, the bilayer capacitance, is measured experimentally and indicates the charge storage capacity at the interface between the electrode surface and the electrolyte [39], excluding any Faradaic reactions. A higher C_{dl} value suggests a larger active surface area, reflecting the surface roughness or electroactive surface area of the electrode. In contrast, C_s provides a standard electric capacity per unit area, serving as a reference for the expected bilayer electric capacity of a known surface area under similar conditions. The ratio of C_{dl} to C_s allows for the estimation of the active surface area of the electrode, providing insight into the electrochemical performance of the TiO_2

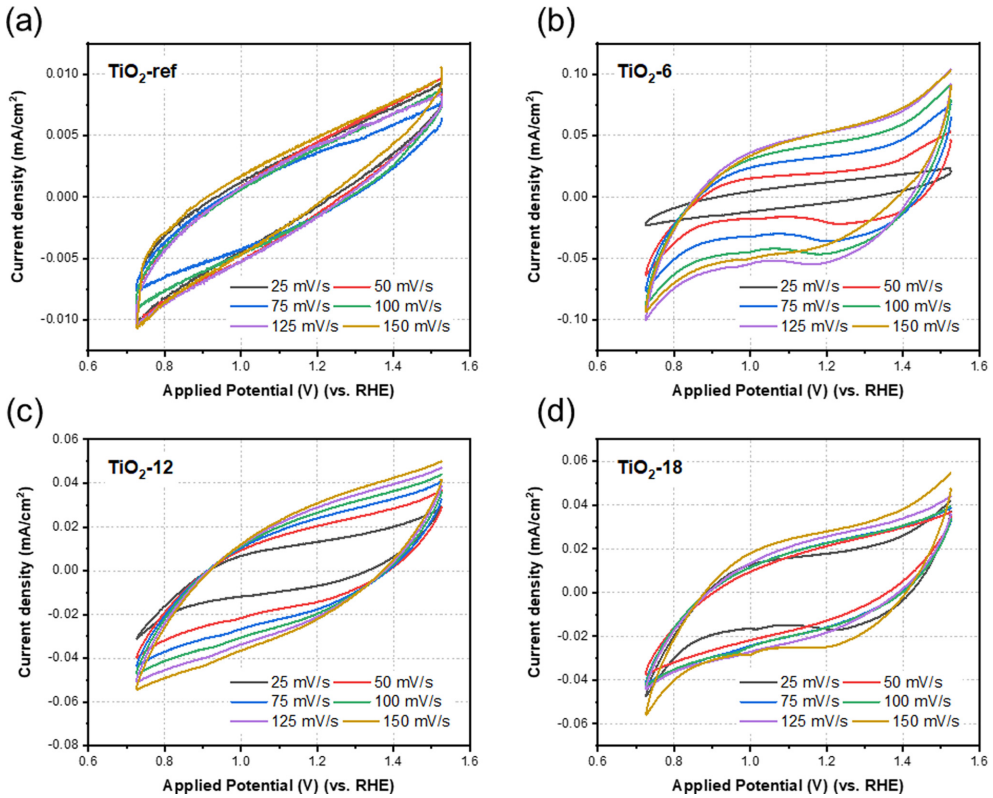

Fig. 4. CVs of TiO_2 nanotube arrays at various scan rates from 25 mV s^{-1} to 150 mV s^{-1}: (a) TiO_2-ref, (b) TiO_2-6, (c) TiO_2-12, and (d) TiO_2-18.

photoanodes produced. This analysis highlights the significance of surface area and roughness in enhancing the electrochemical properties of electrodes for applications such as photocatalysis and PEC water splitting. The CV results are presented in Fig. 4 for various scan rates, and Fig. 5 depicts the calculated ECSA derived from Fig. 4 using Eq. 3 and 4 stated below [40]. CV measurements were repetitively conducted three times for each scan rate, and ΔJ/2 was calculated as the average value of three measurements.

$$C_s = \frac{\int_{V_1}^{V_2} I(V)dV}{mS} \tag{3}$$

$$ECSA = \frac{C_{dl}}{C_s} \tag{4}$$

The C_{dl} value of the TiO_2-6 nanotube arrays was the highest, at 0.241 F cm^{-2}, representing an increase of approximately 34.4 times compared to that of the TiO_2-ref photoanode (0.007 F cm^{-2}). For TiO_2-12 and TiO_2-18 nanotubes, relatively lower C_{dl} values were observed compared to TiO_2-6 nanotubes despite the greater length of the TiO_2 nanotubes. This indicates that the bamboo-type nodes can significantly provide more specific active sites. Therefore, it can be confirmed that the sample with the shortest pulse length exhibits the largest surface area.

The comprehensive PEC performance of TiO_2 nanotubes is evaluated and illustrated in Fig. 6. Fig. 6a displays the chopped on-off photocurrent density as a function of the applied potential for TiO_2 nanotubes. The TiO_2-6 photoanodes achieve photocurrent densities up to 3.5 times higher than TiO_2-ref photoanodes. Furthermore, the onset potential (V_{on}) of bamboo-type TiO_2 nanotubes shifts negatively from 0.4 V_{RHE} to 0.2 V_{RHE}, possibly due to passivation from defect or trap sites in the interfacial region. This marked increase in photocurrent density and the negative shift in V_{on} for TiO_2-6 photoanodes underscore the critical impact of nano structuring and surface

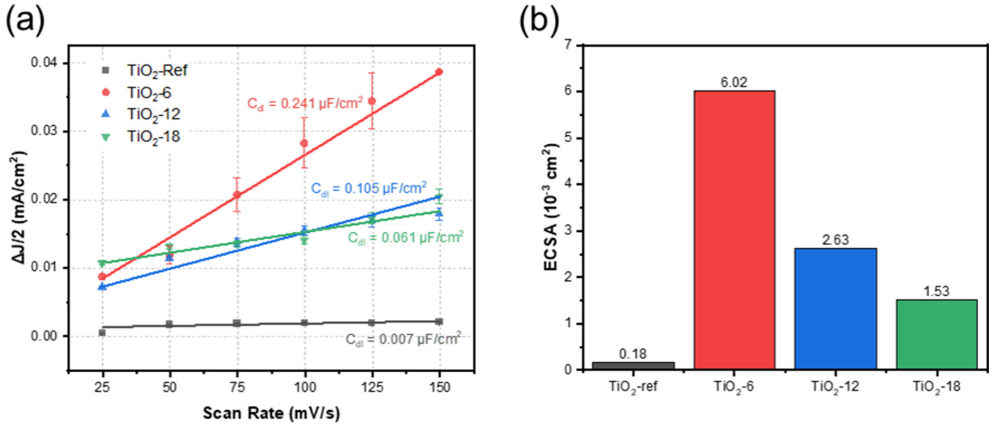

Fig. 5. (a) Half the difference in current density (J) at the center of the CV potential window vs. scan rates for TiO_2 nanotube arrays, and (b) calculated ECSA values.

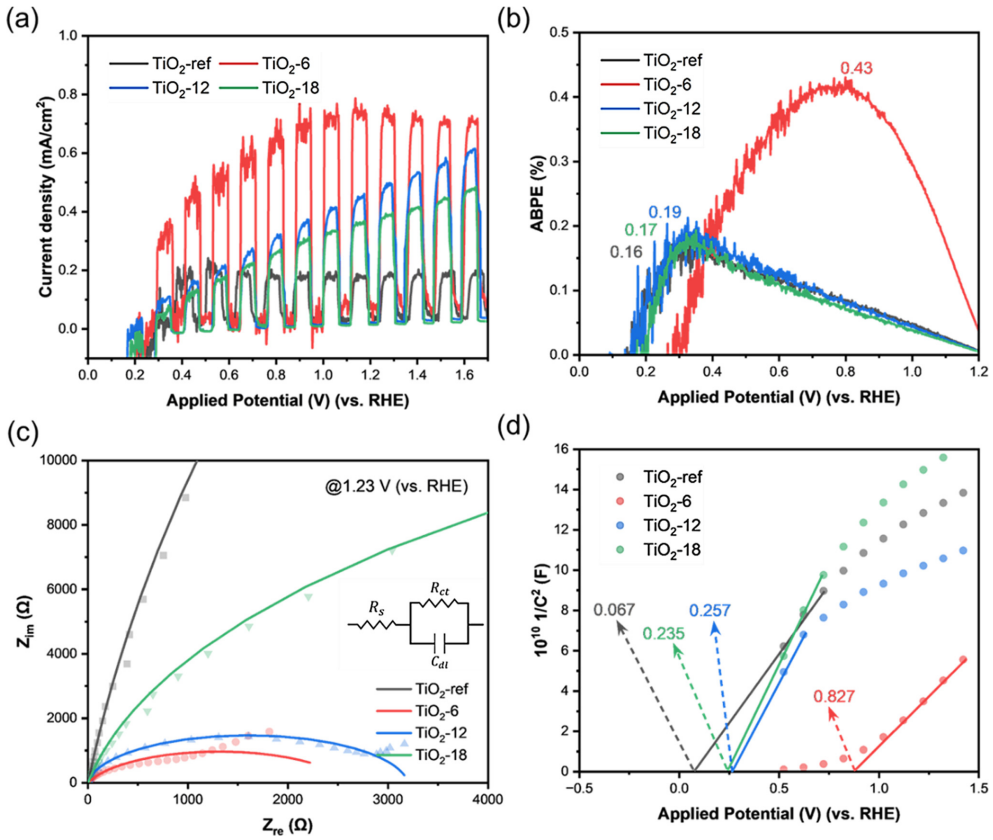

Fig. 6. Comprehensive PEC characterization of TiO_2 nanotubes: (a) photocurrent density measurements, (b) applied bias photon-to-current efficiency (ABPE) curve, (c) EIS Nyquist plots, and (d) Mott-Schottky analysis.

modification strategies on enhancing the PEC properties of TiO_2.

The ABPE was calculated to elucidate the photoconversion efficiency of the TiO_2-based photoan-

odes, using Eq. 5 for this calculation [41,42]. The results are presented in Fig. 6b, highlighting the efficiency of each photoanode under applied bias versus RHE.

$$ABPE(\%) = \frac{J(mA\,cm^{-2}) \times (1.23 - V_{app})(V)}{P_{light}(mW\,cm^{-2})} \times 100 \quad (5)$$

The TiO_2-6 photoanodes exhibit the highest ABPE, demonstrating their superior PEC activity. Specifically, at an applied potential of 0.7 V_{RHE}, TiO_2-6 achieved an ABPE of 0.43%, significantly surpassing other photoanodes. In contrast, the TiO_2-ref, TiO_2-12, and TiO_2-18 photoanodes displayed maximum efficiency at 0.35 V_{RHE}, with efficiencies of 0.16% and 0.19%, respectively. This indicates that TiO_2-6 not only enhances charge separation and transfer, as evidenced by its higher photocurrent density, but also converts a larger fraction of incident photon energy into electrical energy, underscoring its effective PEC water-splitting capability. Fig. 6c shows a Nyquist plot from EIS measurements, which is crucial for understanding the charge transfer properties of the TiO_2 photoanodes. These plots are essential for our detailed investigation to optimize key electrochemical kinetics to boost PEC water-splitting performance. The charge transfer resistance (R_{CT}) results are systematically summarized in Table S1, offering a quantitative comparison of the photoanodes. The TiO_2-ref photoanode exhibits a notably high resistance of 240,000 Ω cm^{-2}, indicating significant barriers to charge movement across the electrode/electrolyte interface. This high resistance likely leads to increased charge recombination rates, thus hindering overall PEC performance. In stark contrast, the TiO2-6 photoanode shows a much lower resistance of 2,615 Ω cm^{-2}, indicating enhanced electrochemical activity and improved charge carrier mobility, favorable for efficient PEC operations. Similarly, the TiO_2-12 demonstrates a resistance of 3,196 Ω cm^{-2}, showing better charge transfer efficiency than the reference model. Meanwhile, TiO_2-18 exhibits a resistance of 29,000 Ω cm^{-2}, lower than the reference but higher than that of TiO_2-6 and TiO_2-12, reflecting its intermediate electrochemical performance.

The semicircular diameters in the Nyquist plots are directly correlated with the charge transfer resistance (Rct) [43–45]. A clear trend of decreasing Rct is observed from the TiO_2-ref photoanodes to the TiO_2-6 photoanodes, signifying a systematic enhancement in electrochemical reactivity. The TiO_2-6 photoanode, in particular, exhibits the most favorable charge transfer conditions due to possessing the lowest Rct among the variants studied. Reducing charge transfer resistance is critical for facilitating efficient transfer from the photoanode to the electrolyte, which is essential for effective PEC water splitting. This enhanced charge transfer efficiency underscores the success of the modifications made to the TiO_2-6 photoanode, highlighting the potential for further optimizations in photoanode design to improve PEC water splitting.

The Mott–Schottky analysis was conducted under dark conditions concerning the applied potential (vs. RHE). Fig. 6d presents the Mott-Schottky plot, deriving the slope of the curves and calculating the charge carrier density (N_d) for TiO_2 nanotube photoanodes. The N_d was determined from the slope and intercept of the Mott-Schottky plot using the following Eq. 6 [46,47].

$$\frac{1}{C^2} = \left(\frac{2}{q\varepsilon_0\varepsilon N}\right)\left(V_{app} - V_{fb} - \frac{kT}{q}\right) \quad (6)$$

where ε_o is the permittivity of a vacuum, ε is the dielectric constant of the semiconductor, and kT/q is the temperature-dependent term. These key parameters, including the N_d and flat band potential (E_{fb}), are summarized in Table S2, providing a comprehensive overview of the TiO_2 nanotube photoanodes for PEC water splitting [48]. Specifically, the TiO_2-6 photoanode, with a slope of 9.07×10^{10}, shows a higher N_d of 7.77×10^{19} cm^{-3} compared to the TiO_2 control sample. This increased N_d implies a higher concentration of charge carriers, which can significantly improve PEC performance by promoting more effective charge separation and minimizing charge recombination [36,49]. Furthermore, the TiO_2-6 exhibits a notably higher E_{fb} of 0.83 V, indicating a more favorable energetic alignment for charge transfer processes [36,50]. These N_d and E_{fb} changes reflect variations in PEC properties across the different TiO_2 NT photoanodes, directly influencing their efficiency in PEC applications.

4. Conclusions

This study thoroughly explains TiO_2 photoanodes fabricated under various anodization conditions to

enhance PEC water-splitting efficiency. The 1D TiO_2 nanotubes were developed using a facile electrochemical anodization process by adjusting pulse anodization parameters. A bamboo-type nanostructure was formed by repeatedly applying an on-off voltage cycle of 60 V and 20 V. The 1D TiO_2 nanotube arrays exhibited different morphological, optical, and PEC properties depending on the off-time, which ranged from 6 min to 18 min. Notably, the TiO_2-6 photoanode, which had the highest ECSA, exhibited excellent PEC performance, achieving a J_{ph} up to 3.5 times higher, compared to the TiO_2-ref photoanode, with a negative shift in V_{on} of approximately 0.2 V. This result underscores the critical role of ECSA in enhancing light absorption, charge separation, and transfer at the electrode/electrolyte interface. EIS measurements further support this finding, showing that TiO_2-6 had the lowest charge transfer resistance, indicating better electrochemical reactivity. Additionally, the Mott-Schottky analysis offers valuable insights into the energy band alignment of the photoanodes, with TiO_2-6 displaying the highest carrier density. These results emphasize the significance of electrode surface properties and energy band positions, such as ECSA and charge transfer resistance, for high-performance PEC photoanodes. Furthermore, this study demonstrates that PEC water-splitting efficiency can be significantly enhanced through controlled anodization conditions, paving the way for the development of efficient and sustainable hydrogen production methods.

Acknowledgments

This study was financially supported by Chonnam National University (Grant number: 2024-1162-01).

References

[1] P. Nejat, F. Jomehzadeh, M. M. Taheri, M. Gohari, and M. Z. A. Majid, *Renew. Sustain. Energy Rev.*, **2015**, *43*, 843–862.
[2] L. J. Minggu, W. R. W. Daud, and M. B. Kassim, *Int. J. Hydrogen Energy*, **2010**, *35(11)*, 5233–5244.
[3] J. Joy, J. Mathew, and S. C. George, *Int. J. Hydrogen Energy*, **2018**, *43(10)*, 4804–4817.
[4] C. Seong, H. Ryu, H. Rho, H. Bae, P. Mane, S. H. Lee, and J.-S. Ha, *Catal. Sci. Technol.*, **2023**, *13*, 4378–4386.
[5] P. Mane, I. V. Bagal, H. Bae, V. V. Burungale, C. Seong, S.-W. Ryu, and J.-S. Ha, *Adv. Sustain. Syst.*, **2022**, *6(6)*, 2200014.
[6] J.-N. Nian, C.-C. Hu, and H. Teng, *Int. J. Hydrogen Energy*, **2008**, *33(12)*, 2897–2903.
[7] Z. Yu, H. Liu, M. Zhu, Y. Li, and W. Li, *Small*, **2021**, *17(9)*, 1903378.
[8] M. Zu, X. Zhou, S. Zhang, S. Qian, D.-S. Li, X. Liu, and S. Zhang, *J. Mater. Sci. Technol.*, **2021**, *78*, 202–222.
[9] N. Celebi, M. Y. Aydin, F. Soysal, Y. O. Ciftci, and K. Salimi, *J. Alloys Compd.*, **2021**, *860*, 157908.
[10] A. Ansón-Casaos, J. Hernández-Ferrer, L. Vallan, H. Xie, M. Lira-Cantú, A. M. Benito, and W. K. Maser, *Int. J. Hydrogen Energy*, **2021**, *46(22)*, 12180–12191.
[11] Y. Liu, M. Wang, B. Zhang, D. Yan, and X. Xiang, *ACS Catal.*, **2022**, *12(12)*, 6946–6957.
[12] O. F. Aldosari and I. Hussain, *Int. J. Hydrogen Energy*, **2024**, *59*, 958–981.
[13] M. H. Sawal, A. A. Jalil, N. F. Khusnun, N. S. Hassan, and M. B. Bahari, *Electrochim. Acta*, **2023**, *467*, 143142.
[14] J. E. Yoo and K. Lee, *Curr. Opin. Colloid Interface Sci.*, **2023**, *63*, 101672.
[15] P. Li, S. Dai, D. Dai, Z. Zou, R. Wang, P. Zhu, K. Liang, F. Ge, and F. Huang, *Chem. Phys. Lett.*, **2023**, *826*, 140675.
[16] L. Liu, K. Hou, Z. Zhang, S. Wang, B. Guo, Z. Jiao, and M. Han, *J. Alloys Compd.*, **2023**, *962*, 171193.
[17] Y. Lin, Q. Qian, Z. Chen, P. D. Tuan, and D. Feng, *Electrochem. Commun.*, **2022**, *136*, 107234.
[18] Q. Qian, Y. Lin, Z. Xiong, P. Su, D. Liao, Q. Dai, L. Chen, and D. Feng, *Electrochem. Commun.*, **2022**, *135*, 107201.
[19] Y. Sun and K.-P. Yan, *Int. J. Hydrogen Energy*, **2014**, *39(22)*, 11368–11375.
[20] X. Zhong, D. Yu, Y. Song, D. Li, H. Xiao, C. Yang, L. Lu, W. Ma, and X. Zhu, *Mater. Res. Bull.*, **2014**, *60*, 348–352.
[21] S. Fatima, I. H. Sajid, M. F. Khan, and S. Rizwan, *Int. J. Hydrogen Energy*, **2024**, *55*, 110–117.
[22] M. A. Alam, R. K. Bishwas, S. Mostofa, and S. A. Jahan, *Mater. Lett.*, **2024**, *354*, 135396.
[23] H. Sopha, Z. Spotz, M. Sepúlveda, M. Alijani, M. Motola, L. Hromadko, and J. M. Macak, *Ceram. Int.*, **2023**, *49(14)*, 24293–24301.
[24] J. Wu, Y. Luo, and Z. Qin, *Constr. Build. Mater.*, **2023**, *408*, 133805.
[25] S. T. Nishanthi, E. Subramanian, B. Sundarakannan, and D. P. Padiyan, *Sol. Energy Mater. Sol. Cells*, **2015**, *132*, 204–209.
[26] Q. Zhang, V. Celorrio, K. Bradley, F. Eisner, D. Cherns, W. Yan, and D. J. Fermín, *J. Phys. Chem. C*, **2014**, *118(31)*, 18207–18213.
[27] A. E. Mesoudy, D. Machon, A. Ruediger, A. Jaouad, F. Alibart, S. Ecoffey, and D. Drouin, *Thin Solid Films*, **2023**, *769*, 139737.
[28] S. Guan, Y. Cheng, L. Hao, H. Yoshida, C. Tarashima, T. Zhan, T. Itoi, T. Qiu, and Y. Lu, *Sci. Rep.*, **2023**, *13*, 14105.

[29] A. Welte, C. Waldauf, C. Brabec, and P. J. Wellmann, *Thin Solid Films*, **2008**, *516(20)*, 7256–7259.
[30] E. Montakhab, F. Rashchi, and S. Sheibani, *Appl. Surf. Sci.*, **2020**, *534*, 147581.
[31] C. A. Grimes and G. K. Mor, *TiO_2 nanotube arrays: Synthesis*, *properties*, *and applications*, Springer Science & Business Media, **2009**.
[32] P. R. Dev, T. M. David, S. J. S. Justin, P. Wilson, and A. Palaniappan, *J. Nanopart. Res.*, **2020**, *22*, 56.
[33] S. K. Kuriechen, S. Murugesan, and S. P. Raj, *J. Catal.*, **2013**, *2013*, 104019.
[34] F. Z. Haque, R. Nandanwar, and P. Singh, *Optik*, **2017**, *128*, 191–200.
[35] P. Prasannalakshmi, N. Shanmugam, and A. S. Kumar, *J. Appl. Electrochem.*, **2017**, *47*, 889–903.
[36] K. Arifin, R. M. Yunus, L. J. Minggu, and M. B. Kassim, *Int. J. Hydrogen Energy*, **2021**, *46(7)*, 4998–5024.
[37] X. Shang, K.-L. Yan, Y. Rao, B. Dong, J.-Q. Chi, Y.-R. Liu, X. Li, Y.-M. Chai, and C.-G. Liu, *Nanoscale*, **2017**, *9*, 12353–12363.
[38] S. I. P. Bakovic, P. Acharya, M. Watkins, H. Thornton, S. Hou, and L. F. Greenlee, *J. Catal.*, **2021**, *394*, 104–112.
[39] S. Zhao, H. Yu, R. Maric, N. Danilovic, C. B. Capuano, K. E. Ayers, and W. E. Mustain, *J. Electrochem. Soc.*, **2015**, *162*, F1292.
[40] P. Connor, J. Schuch, B. Kaiser, and W. Jaegermann, *Zeitschrift für Physikalische Chemie*, **2020**, *234(5)*, 979–994.
[41] S. Wang, P. Chen, J.-H. Yun, Y. Hu, and L. Wang, *Angew. Chem. Int. Ed.*, **2017**, *56(29)*, 8500–8504.
[42] P. Mane, V. V. Burungale, H. Bae, C. Seong, J. Heo, S. H. Kang, and J.-S. Ha, *J. Power Sources*, **2024**, *591*, 233832.
[43] Y. Li, L. Zhang, X. Xiang, D. Yan, and F. Li, *J. Mater. Chem. A*, **2014**, *2*, 13250–13258.
[44] A. Dey, G. Chandrabose, L. A. O. Damptey, E. S. Erakulan, R. Thapa, S. Zhuk, G. K. Dalapati, S. Ramakrishna, N. S. J. Braithwaite, A. Shirzadi, and S. Krishnamurthy, *Appl. Surf. Sci.*, **2021**, *541*, 148571.
[45] X. Zhong, Y. Song, A. Cui, X. Mu, L. Li, L. Han, G. Shan, and H. Liu, *Appl. Surf. Sci.*, **2022**, *591*, 153197.
[46] S. Rai, A. Ikram, S. Sahai, S. Dass, R. Shrivastav, and V. R. Satsangi, *Renew. Energy*, **2015**, *83*, 447–454.
[47] N. SATO, *Tetsu-to-Hagane*, **1990**, *76(9)*, 1423–1436.
[48] M. C. K. Sellers and E. G. Seebauer, *Thin Solid Films*, **2011**, *519(7)*, 2103–2110.
[49] F. Fabregat-Santiago, E. M. Barea, J. Bisquert, G. K. Mor, K. Shankar, and C. A. Grimes, *J. Am. Chem. Soc.*, **2008**, *130(34)*, 11312–11316.
[50] K. Shankar, J. I. Basham, N. K. Allam, O. K. Varghese, G. K. Mor, X. Feng, M. Paulose, J. A. Seabold, K.-S. Choi, and C. A. Grimes, *J. Phys. Chem. C*, **2009**, *113*, 6327–6359.